



# Real-time line-field optical coherence tomography for cellular resolution imaging of biological tissue

KAI NEUHAUS,<sup>1</sup> SHANJIDA KHAN,<sup>1,2</sup> OMKAR THaware,<sup>1,2</sup>  
SHUIBIN NI,<sup>1,2</sup> MINI AGA,<sup>1</sup> YALI JIA,<sup>1,2</sup> TRAVIS REDD,<sup>1</sup> SIYU  
CHEN,<sup>1,2</sup> DAVID HUANG,<sup>1,2</sup> AND YIFAN JIAN<sup>1,2,\*</sup>

<sup>1</sup>Casey Eye Institute, Oregon Health & Science University, Portland, OR 97239, USA

<sup>2</sup>Department of Biomedical Engineering, Oregon Health & Science University, Portland, OR 97239, USA

\*jian@ohsu.edu

**Abstract:** A real-time line-field optical coherence tomography (LF-OCT) system is demonstrated with image acquisition rates of up to 5000 B-frames or 2.5 million A-lines per second for 500 A-lines per B-frame. The system uses a high-speed low-cost camera to achieve continuous data transfer rates required for real-time imaging, allowing the evaluation of future applications in clinical or intraoperative environments. The light source is an 840 nm super-luminescent diode. Leveraging parallel computing with GPU and high speed CoaXPress data transfer interface, we were able to acquire, process, and display OCT data with low latency. The studied system uses anamorphic beam shaping in the detector arm, optimizing the field of view and sensitivity for imaging biological tissue at cellular resolution. The lateral and axial resolution measured in air were 1.7  $\mu\text{m}$  and 6.3  $\mu\text{m}$ , respectively. Experimental results demonstrate real-time inspection of the trabecular meshwork and Schlemm's canal on *ex vivo* corneoscleral wedges and real-time imaging of endothelial cells of human subjects *in vivo*.

© 2024 Optica Publishing Group under the terms of the [Optica Open Access Publishing Agreement](#)

## 1. Introduction

While all OCT methods are based on low-coherence interferometry and obtain a 3D representation of the imaged sample volume, many different variants of methods have been developed regarding scanning and illumination geometries. The most straightforward illumination geometry is to focus the beam from the light source to a small spot. Consequently, the scanning of the spot must traverse laterally a 2D field and axial scanning to obtain the third dimension [1]. Mechanical axial scanning using a reference scanning mirror is referred to as time-domain OCT (TD-OCT) and is nowadays rarely used due to the shallow axial scan range and limited scan speed. To achieve reasonable axial scan speeds, oscillating scanning reference mirrors must compromise between scan speed and range. The scan range reduces significantly at higher scan speeds and is a few hundred micrometers at scan frequencies in the kilohertz range. Axial scanning can also be achieved by Fourier transformation with a spectrometer in the detector arm of the interferometer called spectral-domain OCT (SD-OCT) or a swept laser light source able to rapidly change the emission frequency called swept-source OCT (SS-OCT).

Nevertheless, all three OCT variants use point scanning to traverse a focused illumination spot over the sample to raster a 2D area and reconstruct the imaged 3D sample volume with suitable signal processing steps. Single point 2D scanning OCT variants are sufficient for many applications and are implemented in many commercial OCT systems. They have the disadvantage that phase variations (phase jitter) between each point scan (A-line) can introduce motion artifacts thus reducing resolution and sensitivity. Point scanning often provides limited results despite high scan speeds, especially if it is required to detect cellular and vascular spatiotemporal features *in vivo* for patients that cannot be stabilized with conventional headrests [2–4]. Consequently, in

the past years, further research included the investigation of line and full-field illumination to acquire either a one-dimensional line of axial scans in parallel or all axial scans in a 2D lateral field. The advantages would be the reduction of optomechanical scanning with galvo mirrors and the resulting reduced phase jitter between A-lines, promising improved image quality and simplified construction.

A more comprehensive overview of reported line-field (LF-OCT) and full-field OCT (FF-OCT) variants, including advantages and disadvantages, is provided in literature such as Lawman et al. and Leitgeb et al. [5,6]. Time-domain FF-OCT suffers similar disadvantages compared to single-point scanning time-domain systems using optomechanical axial scanning [7,8], reducing scan speed, achievable imaging depth, and sensitivity. Replacing the light source with a swept laser light source eliminates optomechanical scanning, and a Fourier-domain FF-OCT or full-field swept-source OCT (FF-SS-OCT) can be realized [9]. An improved FF-OCT system was reported with a 3D resolution of  $640 \times 24 \times 512$  voxels, an acquisition time of 10 ms, and a sensitivity of 72 dB, suitable to image retinal structures of the human eye. Nevertheless, the performance gain comes with costs and increased complexity related to achieving sufficient high sweep rates to avoid image blurring that consequently requires camera speeds beyond thousands of image frames per second [10]. Moreover, the sensitivity can be severely impacted by cross-talk, and additional hardware in the attempt to reduce cross-talk makes the system construction increasingly complex [9].

In contrast, line-field OCT (LF-OCT) does not illuminate the full 2D *en face* of the sample but instead scans a line using a galvo mirror. The use of a galvo mirror is causing the already described limitations of scan speeds due to the mechanical nature of the scanning system. Despite the limitations compared to FF-OCT, the LF-OCT method nevertheless provides some advantages that make it attractive to investigate. Although spatially incoherent light allows cross-talk free FF-OCT the implementation is increasingly complex and imaging speed will be impaired depending on the used methodology to reduce spatial coherence. The sequential scan approach simplifies the detection of the interferometric signal using a spectrometer and 2D camera: the interferometer can use a confocal slit to reject out-of-focus light, and the one-dimensional line illumination has reduced crosstalk artifacts compared to FF-OCT. Moreover, using conventional super-luminescent diode (SLED) light sources further reduces integration complexity and cost. Achievable scan speeds are on par with FF-OCT systems, allowing imaging of unstable samples or patients that cannot be stabilized sufficiently.

For ophthalmic imaging systems, the increasing amount of scientific literature suggests rapid progress for high-speed system applications [11–18]. Specific demand for high-speed systems is relevant for treating non-compliant subjects such as infants, children [19], older adults [20,21], and for intraoperative medical applications [22].

Modifying the LF-OCT for a rapid transition from a research grade to a clinical and intraoperative system poses additional challenges in balancing costs and system design. In this study, using a SLED light source and a low-cost camera, real-time imaging with 5000 B-frames per second, continuous real-time imaging was demonstrated [23,24]. Initial results related to anamorphic beam shaping in the detector arm [14] in conjunction with the line-shaping at the objective lens demonstrate sufficient sensitivity for corneal imaging. **Visualization 1** demonstrates that cellular detection is possible in real-time even without image stabilization.

As an example, typical research-grade LF-OCT systems [18] document the use of super-continuum light sources and camera technologies that have an estimated price bracket of tens of thousands of US dollars each.

The system described in this manuscript is novel in its ability to produce medically relevant images using light sources and a camera with reduced costs and real-time image update rates of continuous 5000 B-frames per second. The light source and camera have a smaller form factor, making designing systems for clinical environments easier. Consequently, the image quality is

expected to be at most that of research-grade systems due to the lower hardware specifications and reduced post-processing to sustain real-time imaging capabilities. The high-resolution high-NA sample lens limits the depth of focus, and only a smaller portion of a B-frame can be in focus at a time. However, with the continuous high image update rates, moving the focal layer to the depth of interest can be observed in real time. For still images, the narrow depth of focus is visible in Figs. 4, 7, and 9. Nevertheless, the operator can traverse the confocal layer and inspect it in real-time by shifting *ex vivo* samples with a translational stage along the depth. For *in vivo* imaging, the headrest position can be changed to positions of a specific focal depth of interest while inspecting the video stream (see supplementary Visualization material).

This study contributes essential knowledge about the interplay of sensitivity, resolution, and imaging speed required to outline the next steps for developing commercial clinical-grade systems. The higher speed allows for real-time monitoring that may be relevant for surgical procedures or detecting dynamic processes. Moreover, the additional data acquired due to high data transfer rates allows advanced analytical image processing, such as image stabilization, speckle variance, or numerical refocusing.

## 2. Methods

### 2.1. System design

The real-time LF-OCT system is designed with four cylindrical lenses: two (CL1 and CL2) for the formation of the line-field in the sample and reference arm and two (CL3 and CL4) for anamorphic beam shaping in the spectrometer arm (Fig. 1). The beam splitter (BS) splits the powers equally (50/50) into the reference and sample arm. The focal length of 100 mm for both cylindrical lenses (CL1/2) provide a good compromise to accommodate optical components along the optical path and focusing power on the sample and the spectrometer. The reference arm contains a steering mirror M, variable ND filter and dispersion compensation (DC), a lens (L4) with a 50 mm focal length, and the reference mirror (RM). The sample arm was designed with a beam-expanding lens combination L1 ( $f = 100$  mm) and L2 ( $f = 200$  mm).

The sample illumination from the SLED (M-S-840-B-I-15, Superlum Diodes Ltd.) with a center wavelength of 840 nm ( $\lambda_0$ ) and a bandwidth of 50 nm ( $\Delta\lambda$ ), was coupled from fiber to free space with a collimator (RC08FC-P01, Thorlabs), creating a beam diameter of 8.6 mm ( $d$ ) with a maximum power of 21 mW. The cylindrical lens (CL1) asymmetrically changes the beam from a circular to an elliptic shape. At the focal plane, the elliptical beam is focused to a line shape, creating a length corresponding to the beam diameter. Due to beam expansion, the line length at the entrance pupil of the objective lens, OL, (10x Plan Apo NIR Infinity Corrected, Mitutoyo) is close to 17 mm overfilling the entrance aperture of the objective lens. An additional variable lens, EL, (EL-16-40-TC, Optune) was used to adjust the focal point at the sample on demand. The detector arm comprised a 100 mm lens, L3, and the cylindrical lenses, CL3 and CL4, with a focal length of 100 and 200 mm.

The spectral decomposition of the interference was performed with a custom-built spectrometer using a grating, (GT in Fig. 1(a)), with 1800 lines per mm ( $N$ ) and a 2-inch diameter (Wasatch Photonics). The grating allows for a theoretical spectral resolution for the first order ( $d = 1$ ) of  $SR = \lambda_0/d/N = 0.06$  nm. A camera lens (Zeiss Planar 1.4/85 M42-IR) focuses the spectrum onto the camera detection area (EoSens 1.1 CXP2.0, Mikrotron). The camera is specified with a 60 dB dynamic range and about 12 percent quantum efficiency at 840 nm wavelength. The camera was configured in global shutter mode, and the detection area of the detector chip (LUX13HS) was  $1024 \times 500$  out of  $1280 \times 864$  pixels, which provides 500 lateral pixels and 512 axial pixels after fast Fourier transformation (FFT) of the 1024 spectral samples. The 1024 pixel for spectral detection would allow the detection of spectral intervals of  $\Delta\lambda/1024 = 0.05$  nm, providing a sufficient match to the theoretical spectral resolution. The Mitutoyo lens (OL) is specified with an NA = 0.26 [25] and the optical resolution can be estimated by using the center wavelength of

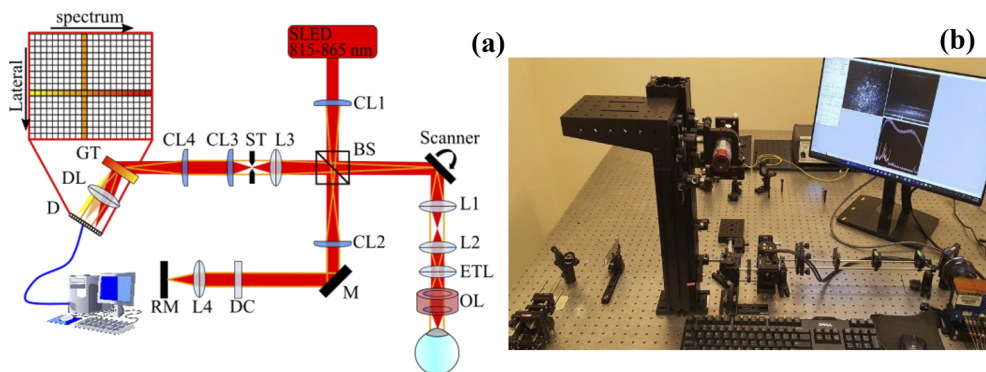


**Fig. 1.** (a) System schematics and (b) hardware setup of the real-time LF-OCT. In schematic (a) the beam is injected with a collimator generating a beam with 4 mm diameter from the SLED. The cylindrical lens (CL1) forms the lateral line illumination passing through the beam splitter (BS) with 50/50 splitting ratio, a second cylindrical lens (CL2), steering mirror (M), variable attenuation and dispersion compensation (DC), the reference lens (L4), and the reference mirror (RM). The sample arm is composed of the scanner, the beam expansion (L1, L2), a liquid lens (ETL), and the sample lens (OTL). The detector arm is comprised of a lens (L3), slit (ST), cylindrical lenses (CL3) and (CL4), the grating (GT), the detector lens (DL), and the detector (D). In (b) the SLED light source is visible in the background. The reference arm and mirror are visible at the lower left, and the spectrometer and high-speed camera at the lower right. The headrest is not shown. The 10X Mitutoyo lens is mounted at the upper right end of the vertical column.

840 nm to be  $\Delta x = 0.37 \cdot \lambda/NA = 1.2 \mu\text{m}$  [26]. The depth of focus (DOF) is twice the Rayleigh range and can be estimated using  $b = 2z_R = \pi\Delta x^2/2\lambda$  to be  $2.7 \mu\text{m}$  [27]. Although the narrow DOF does not allow capturing B-frames over the entire depth range at high resolution, *en face* imaging can still be performed. The high acquisition speed makes capturing high-resolution *en face* images for different DOFs easy.

## 2.2. Data acquisition and processing

The selected signal acquisition components; the CMOS camera (EoSens 1.1CXP2, Mikrotron GmbH) and digitizer (Bitflow, CLX-5.0-00150-CXP4) using the CoaXPress interface with four signal lanes; were chosen to achieve high data rates of up to 12.5 Gbit/s. A suitable main board (ASUS ProArt Z690-CREATOR WiFi) was selected and equipped with an appropriate (Intel Core i9-12900 K) processor with maximum core frequencies of 5.20 GHz and 64 GB RAM. A dedicated graphics processing unit (NVIDIA GeForce RTX 3090) was installed to allow parallel processing of computationally intensive processing tasks such as the FFT. A custom-programmed processing framework (C/C++) was implemented to perform data acquisition, OCT processing, image display, and data storage utilizing the camera's 5000 frames per second [23,28,29]. The delay due to processing was minimal, and the maximum *en face* display rate would be about ten frames per second. In more detail, the OCT processing includes conventional DC subtraction, k-space linearization, dispersion compensation, inverse FFT, intensity thresholding, and adjustable averaging.

Still images presented in this study were extracted from the real-time data and post-processed with ImageJ/Fiji [30], scipy [31], numpy [32], skimage [33], and tomviz [34]. Additional video material in the supplementary Visualization material demonstrates the real-time capabilities of the system described.

### 2.3. Ex vivo sample preparation

Human eyes were obtained from the Oregon Lions Eye Bank (Portland, OR) within 48 hours postmortem. The whole globes were rinsed twice with phosphate-buffered saline (PBS) (ThermoFisher Cat# 10010023) containing 1% pen-strep (ThermoFisher 15140122). Anterior segments were obtained as described previously in Bradley et al. and Johnson et al. [35,36], and maintained in medium-glucose (a 1:1 mix of high- and low-glucose) Dulbecco's Modified Eagle Medium supplemented with 1% antibiotic and antimycotic mix. After 5 days of stationary organ culture, the anterior segment was cut into 6 corneoscleral wedges and fixed for 1 hr. at room temperature using 4% paraformaldehyde and prepared for imaging.

### 2.4. In vivo imaging declaration

The studies involving human participants were reviewed and approved by Oregon Health and Science University Institutional Review Board. Written informed consent to participate in this study was provided by the participants' legal guardian/next of kin. Written informed consent was obtained from the minor(s)' legal guardian/next of kin for the publication of any potentially identifiable images or data included in this article.

## 3. Results

### 3.1. System characterization

The system was characterized by measuring the lateral and axial resolution, the intensity fall-off of the axial point-spread-function (PSF), and the sensitivity. A United States Air Force (USAF 1951) target was imaged, and it was possible to discern structures corresponding to group 8 and element 2, which are related to a line width of 1.74  $\mu\text{m}$  or 287.4 lines per millimeter and line spacing of 3.48  $\mu\text{m}$  (Fig. 2(c)).

The system's maximum signal-to-noise ratio (SNR) was estimated based on the shot-noise limit [37–40]. Considering 5000 frames per second, the illumination light source, a sample power of 2.7 mW, and the lateral power distribution of the illumination line, the expected SNR would be about 88 dB. The sensitivity was measured by keeping the injection power of the SLED at its maximum of 21 mW and adjusting the sample power to 2.7 mW, which is lower than the maximum permissible exposure on the human cornea and retina specified by the ANSI Z80.36-2016 [17,41]. The sample mirror was attenuated with an ND filter with an optical density 2 (OD2), attenuating the sample power by 40 dB considering the roundtrip attenuation due to the sample light passing twice through the ND filter. A maximum sensitivity of about 70 dB was measured at the center of the lateral FOV. The measured SNR may be less due to the camera's internal signal conditioning.

The FWHM of the axial PSF was measured by fitting a Gaussian model [42] over an axial range around the peak location, providing a mean peak width of 6.3  $\mu\text{m}$  (Fig. 3(b)). The plot in Fig. 3(c) shows the variance of the PSF over the selected measurement. Evaluating the variance of the FWHM could help detect effects that may impact the resolution vs. axial depth, for example, due to noise in the data or data processing artifacts. In general, we expect that the value of the FWHM only depends on the bandwidth of the light source and should not change along the axial depth in air. The variance of the FWHM can be used to calculate a standard deviation as uncertainty to the mean value of the FWHM =  $6.3 \mu\text{m} \pm 0.6 \mu\text{m}$ . With parameters of  $\lambda = 840 \text{ nm}$  and  $\Delta\lambda = 50 \text{ nm}$ , the theoretical axial resolution  $\Delta z = 2\ln\frac{2}{\pi} \cdot \lambda^2/\Delta\lambda$  has a value of  $\Delta z = 6.23 \mu\text{m}$ , which compares well with the measured value of 6.3  $\mu\text{m}$ . With  $500 \times 500$  lateral *en face* (x, y) and 512 axial pixels along depth (z) the theoretical optical voxel size would be  $(\Delta x, \Delta y, \Delta z) = (1.2 \times 1.2 \times 6.2) \mu\text{m}$  and with the measured resolution values  $(1.7 \times 1.7 \times 6.3) \mu\text{m}$ . The fall-off of -6 dB is ideally expected at  $\ln(2/\pi) \cdot \lambda_0^2/\Delta\lambda = 3.1 \text{ mm}$  and was measured at a depth of around 2 mm in the air [26,43].

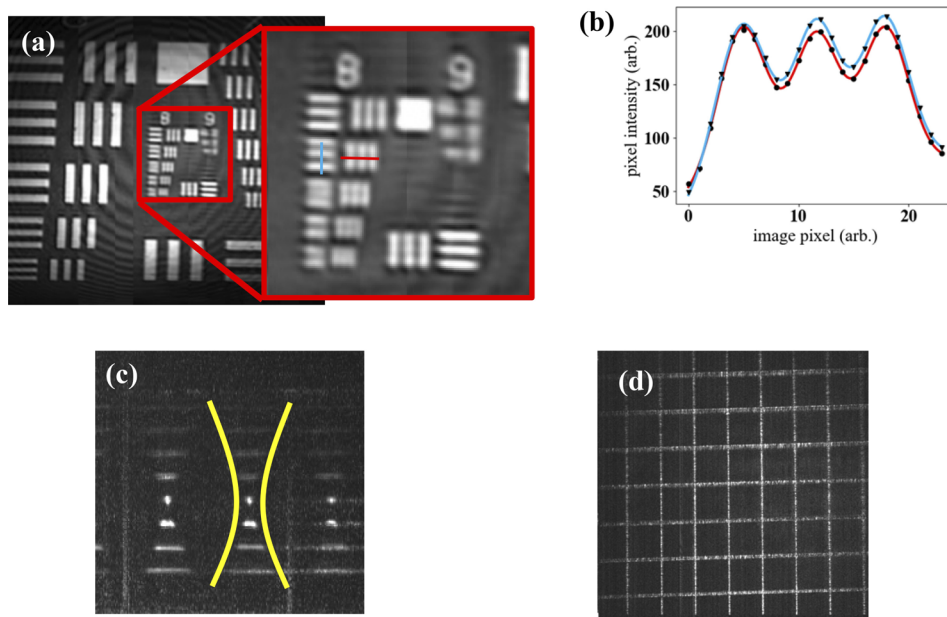


**Fig. 2.** (a) The lateral resolution was measured with a USAF target on element 2 of group 8. The fitted intensities for vertical and horizontal dimensions (markers indicate the pixel values) show that element 2 (b) can be discerned. A line width of 1.74 micrometer can well be identified. The images (c) and (d) were obtained with the 3D grid OCT phantom (Arden Photonics, APL-OP01) to evaluate the confocal gating (yellow) (c), and the lateral field of view ( $700 \times 700$ )  $\mu\text{m}$  (d). The grid size of the phantom is  $(100 \times 100)$   $\mu\text{m}$ , and the vertical spacing between the gird layers is  $75 \mu\text{m}$ .

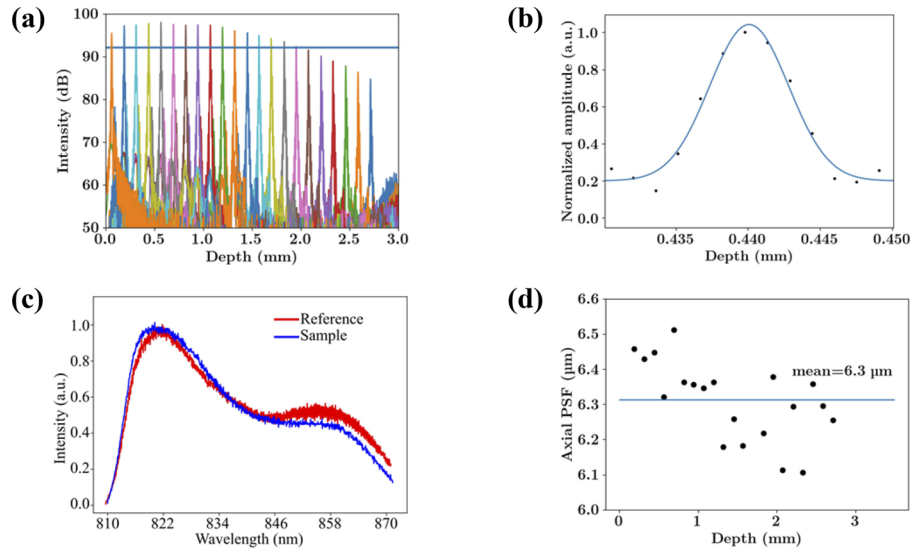


**Fig. 3.** (a) Fall-off characteristic of the unattenuated mirror signal for the axial PSF in air. The -6 dB fall-off (blue line) coincides at a depth of around 2 mm. The focus was positioned around 0.5 mm depth. (b) Gaussian fit for data points at a depth at about 440  $\mu\text{m}$ , (c) the detected spectra for the reference and sample arm, and (d) all values for the FWHM at all measured depth positions, including the mean of 6.3  $\mu\text{m}$ .

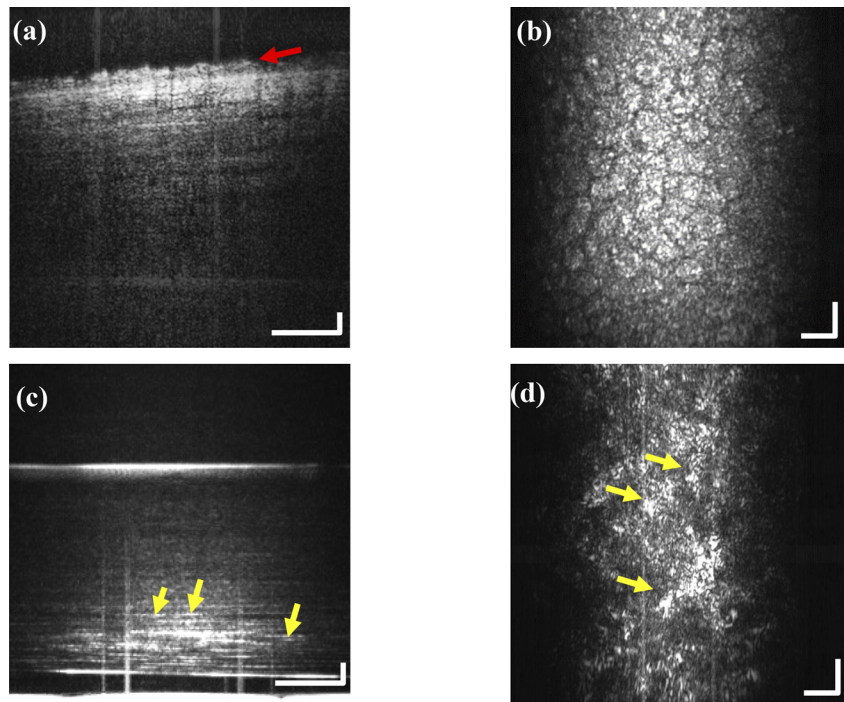


**Fig. 4.** (a) B-frame of a human *ex vivo* corneoscleral sample showing the endothelial layer (red arrow). Note that the endothelial cells are abnormally swollen and appear enlarged. (b) *En face* projection at the same sample position shows the endothelial cells' hexagonal pattern. (c) B-frame of the stroma of the same sample showing the thin and stretched keratocytes (yellow arrows), and (d) the *en face* projection. Note that larger patches may indicate clustering of keratocytes due to deformation of the cornea. The FOV for the B-frames (a) and (c) is about  $(150 \times 500)$   $\mu\text{m}$  (scale bars 30  $\mu\text{m}$ ) in width and height, and for the *en face* images (b) and (d) about  $(300 \times 300)$   $\mu\text{m}$  (scale bars 30  $\mu\text{m}$ ).

### 3.2. Imaging biological tissue

#### 3.2.1. Imaging human *ex vivo* corneoscleral wedge

Studying the dynamic behavior of the trabecular meshwork and Schlemm's canal could be helpful to better understand and find new ways of preventing glaucoma [44,45]. A high-speed imaging system can observe the spatiotemporal response of the structures in real-time and in three dimensions, which is not possible with conventional microscopy.

This section presents image snapshots of real-time imaging of corneoscleral wedges cropped to approximately  $300 \times 300$  micrometers (Fig. 4). [Visualization 1](#) shows that it is possible to track the Schlemm's canal and trabecular meshwork with sufficient detail that would allow the direct measurement of structural changes due to dynamic excitation.

The [Visualization 2](#) demonstrates the observation through different structural depth layers with the real-time LF-OCT, allowing not only the assessment of intricate anatomical structures but also the monitoring of dynamic processes of flow through vessel structures such as the Schlemm's canal. Figure 5 shows still images to the corresponding real-time images.

Tracking the Schlemm's canal is generally challenging due to the highly scattering trabecular mesh and scleral tissue covering it. Nevertheless, the system can help to evaluate the spatiotemporal properties of Schlemm's canal relevant to understanding the biomechanics of the aqueous outflow pathways [46].

### 3.2.2. Imaging of human cornea *in vivo*

Imaging human cornea *in vivo* required minimal preparation using a conventional headrest. The headrest was initially adjusted to position the volunteers' eyes such that the cornea was coarsely aligned with the focal position of the sample lens. Volunteers were asked to stabilize their gaze as much as possible that was most comfortable for them. Although a dedicated visual target could be of advantage for future system iterations, imaging and identifying cellular sized structures was possible without additional aid. Simply asking volunteers to change their gaze was used to image different spots on the cornea and to track nerve fibers. The system has no particular focus tracking or stabilization method, but it was sufficient to get snapshots from endothelial cells. Again, future system iterations can include more sophisticated tracking to improve image acquisition. Notably, despite the volunteers being nearly freely moving, without the requirement to suppress the blink reflex, the acquisition of data volumes at arbitrary intervals controlled by the operator was sufficient to isolate many anatomical structures in the cornea such as endothelial cells (Fig. 6) and keratocytes (Fig. 7). The system would be as is already applicable for clinical imaging without significant additional engineering efforts.

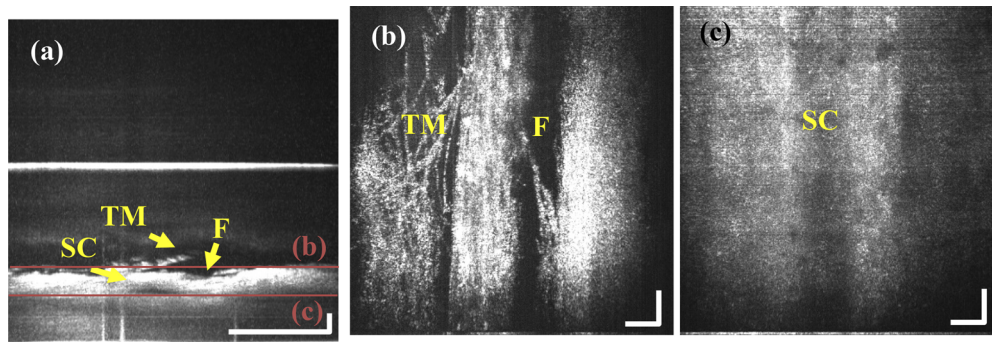


**Fig. 5.** Tracking of the Schlemm's canal. (a) B-frame FOV about  $(200 \times 1000)$   $\mu\text{m}$  (scale bars 60  $\mu\text{m}$ ) showing the layers (maroon colored) used for images (b) and (c). The layer (b) includes the trabecular meshwork (TM) and the layer (c) includes the Schlemm's canal. Note that the fissure (F) in the upper layer (b) is slightly displaced relative to the Schlemm's canal in layer (b). (b) *En face* image from showing the TM from the layer as indicated in (a). (c) *En face* image of the SC below the TM as indicated with layer (c) in subfigure (a). *En face* images (b) and (c) FOV is  $(300 \times 300)$   $\mu\text{m}$  (scale bars 30  $\mu\text{m}$ ).

The image snapshots in this section demonstrate the system's capabilities, and [Visualization 3](#) provides supplementary video material showing imaging in real time. The still images in this section are cropped, and the resulting lateral and depth of view are stated accordingly. The still images demonstrate the identification of endothelial cells, keratocytes, and nerve fibers. Identification of epithelial cells was limited and only some structures were visible that may require further evaluation (Fig. 8(c)). The real-time image display does not yet account for the cornea's curvature along the depth, and only a fraction of endothelial cells is visible laterally. Figure 6 demonstrates imaging of endothelial cells in real-time from two different individuals. It should be noted that different morphological properties, such as size and contrast, originate most likely from different depth positions of the focal plane and the relatively narrow DOF, which can be addressed in future system design iterations using suitable image stabilization methods.

Although the Rayleigh range (focal depth) is shallow due to the high NA objective lens, the depth of field is sufficient to identify the stratified structures of the stroma and the embedded keratocytes (Fig. 7). The difference in morphological features of the keratocytes, such as

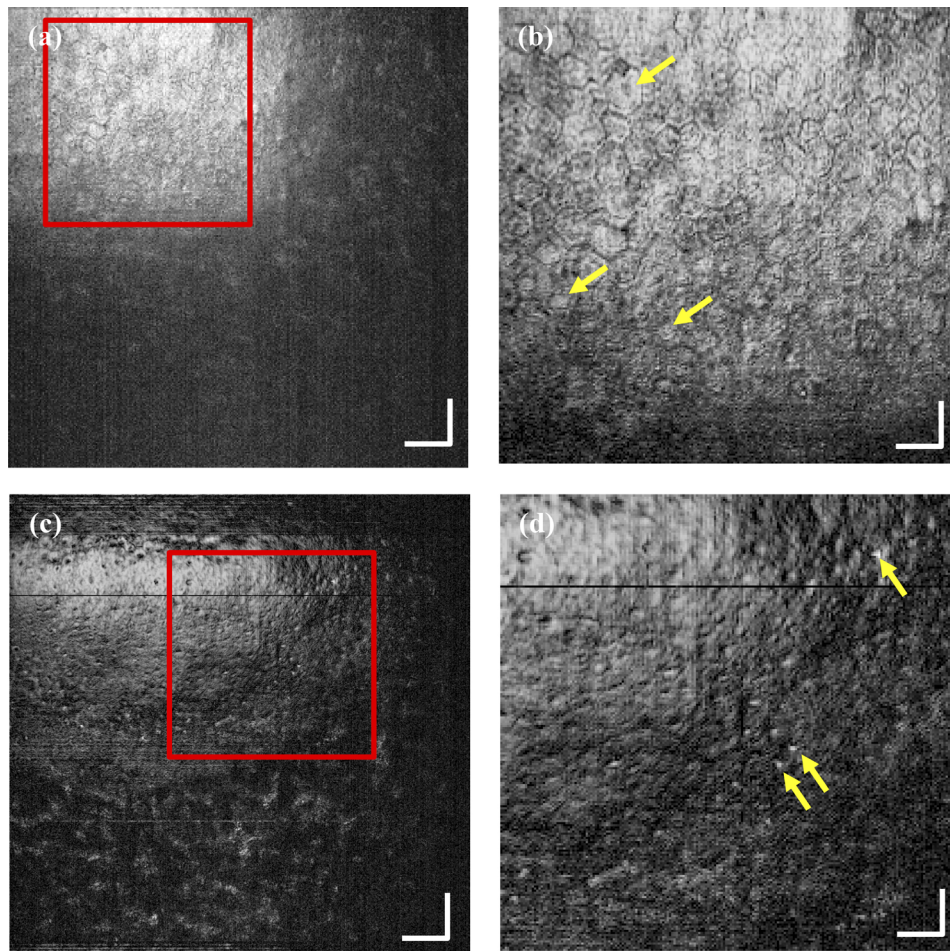


**Fig. 6.** *In vivo* real-time imaging snapshots of endothelial cells from two different human participants. The field of view for the left column of images (a) and (c) is (700 × 700) micrometers (scale bars 70 μm), and the right column (b) and (d) are the zoomed region (red) with a FOV of about (300 × 300) micrometers (scale bars 30 μm). Differences in contrast and cell size between the first participant, subfigure (a) and (b), compared to the second participant, subfigure (c) and (d), originate most likely from different depth positions of the focal plane and the limited DOF. The images for participant (c) and (d) are out of focus and bright spots of artifacts around the endothelial cells become visible (yellow arrows). Because due to the curvature of the cornea we can see how the keratocytes become increasingly visible at the bottom in image (c). Although for the current system configuration no image stabilization was attempted, the high imaging speed allows for multiple snapshots of full 3D image volumes allowing enhanced off-line inspection (see [Visualization 1](#)).

reflectance and size, may be attributed to the uncertainty of adjusting the depth position of the focal plane.

Despite the narrow depth of field of the 10X Mitutoyo lens, it is possible to extract 3D structures of keratocytes and nerve fibers (Fig. 8). Future development of the real-time image and processing framework would allow the inclusion of a direct 3D image representation. However, conventional post-processing to trace, for instance, nerve fibers in 3D is possible with simple techniques.

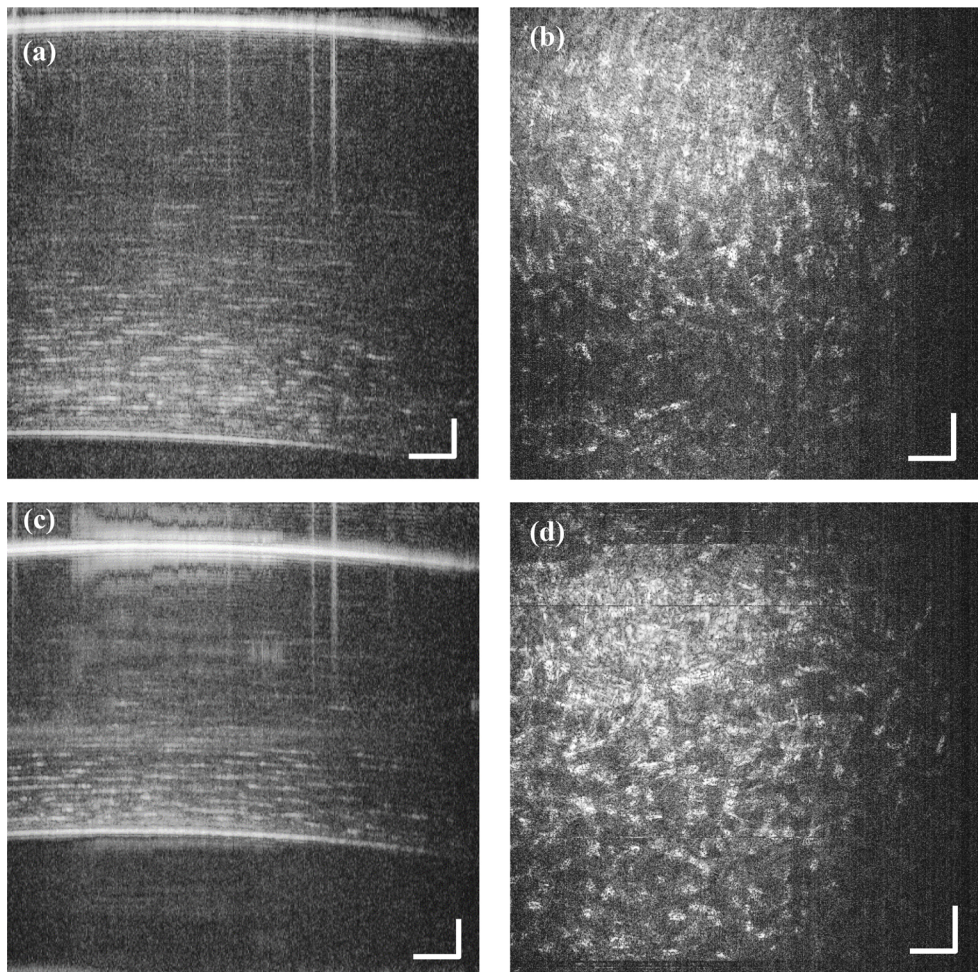


**Fig. 7.** *In vivo* B-frames (a) and (c) from two different participants and corresponding *en face* images (b) and (d), about one hundred micrometers above the endothelial layer showing the distinct star shaped keratocytes. The width and height of the B-frames (a) and (c) is 700 and 800 micrometers respectively (scale bars 70  $\mu\text{m}$ ). The *en face* images have a field of view of 700  $\times$  700 micrometers (scale bars 70  $\mu\text{m}$ ). We can appreciate the thicker (a) vs the thinner cornea (c). The focus for (a) and (c) was adjusted for the endothelial layer which causes increased intensity of the stratified stromal layers and keratocytes at the bottom of the images (a) and (c). Image (d) shows artefacts of horizontal image discontinuities due to occasional incomplete frame captures.

Evaluating magnified regions from the real-time snapshots permits the discrimination of different anatomic structures *in vivo*, such as the corneal epithelium (EP), the basal cell layer (BCL) of the corneal epithelium, the Bowman layer (BM), the stroma (ST), the endothelial layer (EL), and the Descemet's membrane (Fig. 9) [47]. Because the focus is adjusted to the corneal epithelium the Descemet's membrane may be merged with the endothelial layer (Fig. 9(c)).

The *in vivo* images demonstrate that the real-time imaging quality of the investigated LF-OCT is on par compared to many other single-shot systems published. Although higher resolution and sensitivity can be desirable for specific analytical imaging goals, the system provides excellent support in a clinical setting, monitoring anatomical structures during surgery. Also, compared to

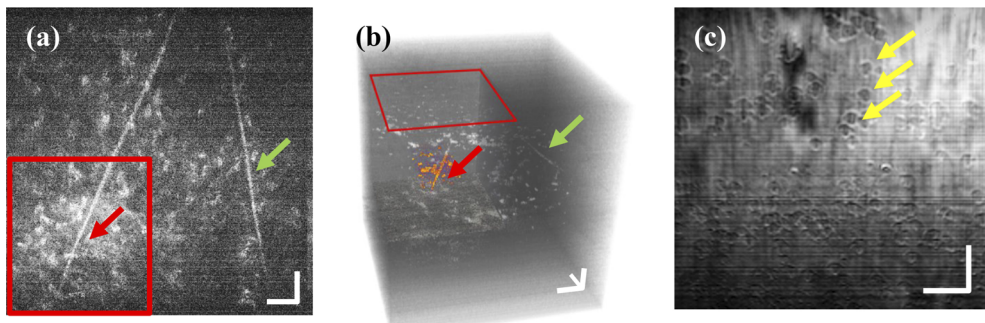


**Fig. 8.** With the focus aligned below the epithelium and closer to the scleral edge we can increasingly identify larger nerve fibers (a) (see [Visualization 4](#)). The dimensions of (a) are  $700 \times 700$  micrometers. With suitable post processing methods, we can allocate the nerve fiber structure in 3D, perform segmentation, and trace the path through the stroma (b). The colored arrows indicate the corresponding two strongly reflecting nerve fibers between the *en face* (a) and the 3D rendering (b). The dimensions of the cube (b) are  $700 \times 700 \times 900$  micrometers. Other structures were observed sporadically (yellow arrows) and are located in the center of the image (c). The field of view for (c) is about  $450 \times 450$  micrometers after cropping. All scale bars are  $70 \mu\text{m}$ .

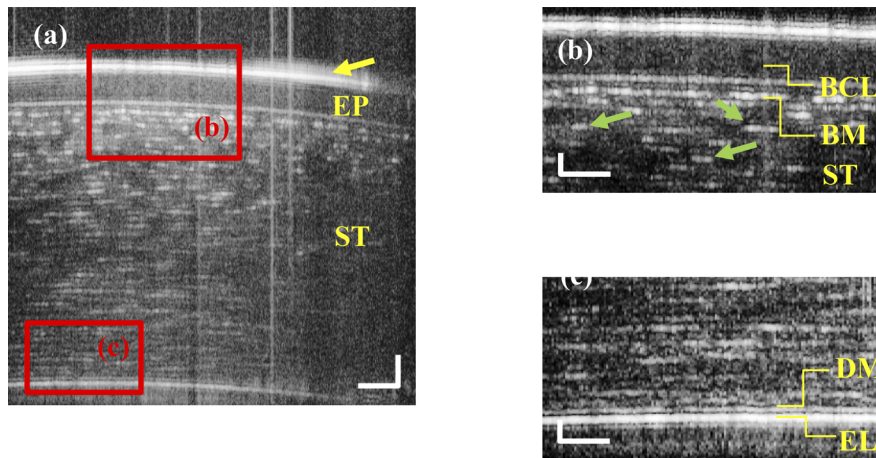


**Fig. 9.** Along the depth of the cornea different anatomical layers can be identified. In (a) the red boxes (b) and (c) are cutouts that are zoomed into in their corresponding figures (b) and (c). The yellow arrow in (a) indicates the highly reflecting tear film, then the corneal epithelium (EP), and the stroma (ST). Subfigure (b) shows a zoomed version with better visibility of the EP, the adjacent basal cell layer (BCL), the Bowman layer (BM), and stroma (ST). Some prominent highly reflecting elongated keratocytes (green arrows) are labeled in subfigure (b). Due to the focus at the epithelial layer the keratocytes towards the endothelial layer appear increasingly elongated. The Descemet's membrane (DM) and the endothelial layer (EL) in (c) may be partially merged and potential side lobe artefacts of the OCT signal may obfuscate some of the layered structures. The FOV for (a) is vertically 900 and laterally 700 micrometers (scale bars  $70 \mu\text{m}$ ), and the zoomed regions (b) and (c) are approximately 220 micrometers vertically and 170 micrometers laterally (scale bars  $25 \mu\text{m}$ ).

other systems, the described LF-OCT setup provides a unique option to image non-compliant subjects where the fixture of the head and eye position is not feasible.

#### 4. Discussion

The principle of the line-field OCT method is well established, and many scientific publications demonstrate its capabilities. This study addresses the technology trajectory to reduce costs and whether components with more limited specifications can lead the way for clinical applications. Moreover, in many cases, single-shot high-speed image acquisition can be sufficient for many application areas; video-rate imaging systems add the capability of evaluating spatiotemporal processes critical to monitoring structural changes over short timeframes. The investigation of the described video-rate LF-OCT system showed that continuous monitoring of cellular structures would benefit from image stabilization. Although image stabilization was not essential for general imaging, it would be, for example, helpful for accurate positioning of the depth location of the focal plane. The increased freedom of the subject's mobility allows the inspection of areas with direct image feedback. It also was shown that the reduced demand of hardware parameters compared to systems with the highest possible sensitivities unlocks the use of a less expensive system design and accelerates the commercialization of the system. Some challenges for future iterations may be the management of the large number of generated data and images, as reviewing recordings can take time and effort. However, this is a suitable task for a machine learning frameworks, and the data volume available could be valuable for training artificial networks for detecting structures of interest, performing automatic snapshots, or disease detection.

The general data processing steps for the described high-speed system are DC subtraction, k-space linearization, fast Fourier transformation, averaging and filtering, and display of *en face* and B-frame slices out of the acquired 3D image volume. At 5000 B-frames per second, a 3D image with 500 B-frames, and ten *en face* frames per second, many problems associated with observing fast-changing processes become accessible, and imaging unstable samples or non-compliant individuals becomes possible. The optical configuration for anamorphic beam shaping is relatively simple, and tuning was possible on demand. Fine-tuning for optimal axial resolution and contrast is generally performed during the alignment procedure. However, there could be some advantages to optimizing the configuration for specific sample structures. The SLED light source reduces costs and causes less system integration efforts. Despite the center wavelength of 840 nm limiting the visibility of endothelial and epithelial cells, the image contrast is sufficient to identify many relevant cell-sized structures. Although a 70 dB sensitivity is not on par with other published systems that can achieve more than 90 dB sensitivity, the described system can detect many anatomically and clinically relevant structures. Because the cornea is almost transparent and scattering is minimal around the used wavelength of 840 nm, we expect that the refractive index change between structures and the peripheral medium is a dominant measure of the visibility. For instance the Bowman's layer is reported with a refractive index of  $n_B=1.38$  and the cornea with  $n_C=1.48$ , a reflectivity for a normal incidence beam would be  $R = \left\{ \frac{n_C-n_B}{n_C+n_B} \right\}^2 = 0.001$  [48]. That means the reflected sample power is 0.001 times less than the incidence power. The value in decibel  $20 \cdot \log_{10}(0.001) = 58$  dB indicates that the relatively weakly reflecting Bowman's layer is detectable with 70 dB. The calculated reflectivity of the Bowman's layer serves as an estimate and may vary due to factors such as the incidence angle of the illumination beam or increased scattering due to disease conditions such as corneal dystrophies and cataract.

The center wavelength of 840 nm and bandwidth of 50 nm was dictated by the light sources to keep the system complexity manageable. The reflectivity of endothelial cells depends on the illumination wavelength and biological origin [49]. Shorter wavelength ranges can provide

higher contrast [50,51]. Other published systems demonstrate imaging of endothelial cells with expensive, more complex light sources such as supercontinuum lasers and extensive post-processing to achieve optimal visibility. The described system provides an excellent platform that can be further engineered toward the next technology readiness level but is also flexible enough to investigate further research questions of either technical or clinical nature.

## 5. Conclusion

The described real-time line-field optical coherence tomography system allows imaging of cellular structures in both *ex vivo* and *in vivo* corneal tissues. The ultra-high imaging speed reduced the need for sample stabilization and allows the imaging of samples in rapid succession or observing dynamic processes. Videos on imaging the trabecular meshwork and Schlemm's canal on *ex vivo* corneoscleral wedges (Section 3) demonstrate the real-time viewing capabilities of the system. *In vivo* imaging was performed on different volunteers. No specific stabilization of the subjects was required to obtain suitable snapshots. It is possible to take multiple snapshots in quick succession from different regions, therefore increasing the system's diagnostic capabilities. With a scanning speed of 5000 B-frames per second corresponding to an A-line rate of 2.5 million lines per second and future optomechanical enhancements imaging of non-compliant subjects such as elderly or infants should become possible. To the best of our knowledge, this is the first high-speed line-field OCT system capable of continuous real-time imaging using off-the-shelf components. The measured sensitivity of 70 dB was sufficient for detecting features and cells *in vivo* in the cornea. Using a USAF target, the measured resolution in air was 1.76 micrometers laterally and  $6.3 \pm 0.6$  micrometers axially. The imaging was performed with sample powers between 1.7 to 2.5 mW, within the safety margin of the maximum permissible exposure. Literature [37] suggests that endothelial cells generate reduced imaging contrast for a center wavelength at 840 nm, as observed in this study. Therefore, it was expected that reliable visualization of epithelial cells is not optimal. Despite the expected reduced contrast of epithelial cells, the described system can reasonably well detect endothelial cells. Tracking keratocytes, nerve fibers, and the stroma allows the evaluation of shapes and densities that could be essential for medical diagnostics. The reduced component costs of the system allow more straightforward enhancements and transition to a commercial-grade development.

**Funding.** Edward N. and Della L. Thome Memorial Foundation; BrightFocus Foundation (M20230081); Research to Prevent Blindness; National Eye Institute (P30 EY010572, R01 EY028755, R01 EY035410, R01HD107494).

**Disclosures.** David Huang: Optovue Inc. (F, I, P, R). These potential conflicts of interest have been reviewed and managed by OHSU. Other authors declare no relevant conflicts of interest related to this article.

**Data availability.** Data underlying the results presented in this paper are not publicly available at this time but may be obtained from the authors upon reasonable request.

## References

1. D. Huang, E. A. Swanson, C. P. Lin, *et al.*, "Optical coherence tomography," *Science* **254**(5035), 1178–1181 (1991).
2. B. Tan, Z. Hosseinaee, L. Han, *et al.*, "250 kHz, 1.5 μm resolution SD-OCT for in-vivo cellular imaging of the human cornea," *Biomed. Opt. Express* **9**(12), 6569–6583 (2018).
3. D. Hillmann, H. Spahr, C. Hain, *et al.*, "Aberration-free volumetric high-speed imaging of in vivo retina," *Sci. Rep.* **6**(1), 35209 (2016).
4. V. Mazlin, P. Xiao, J. Scholler, *et al.*, "Real-time non-contact cellular imaging and angiography of human cornea and limbus with common-path full-field/SD OCT," *Nat. Commun.* **11**(1), 1868 (2020).
5. S. Lawman, Z. Zhang, Y.-C. Shen, *et al.*, "Line Field Optical Coherence Tomography," *Photonics* **9**(12), 946 (2022).
6. R. A. Leitgeb, "En face optical coherence tomography: a technology review [Invited]," *Biomed. Opt. Express* **10**(5), 2177 (2019).
7. E. Beaurepaire, A. C. Boccara, M. Lebec, *et al.*, "Full-field optical coherence microscopy," *Opt. Lett.* **23**(4), 244–246 (1998).
8. H. Sudkamp, P. Koch, H. Spahr, *et al.*, "In-vivo retinal imaging with off-axis full-field time-domain optical coherence tomography," *Opt. Lett.* **41**(21), 4987–4990 (2016).
9. E. Auksorius, D. Borycki, and M. Wojtkowski, "Crosstalk-free volumetric in vivo imaging of a human retina with Fourier-domain full-field optical coherence tomography," *Biomed. Opt. Express* **10**(12), 6390–6407 (2019).

10. T. Bonin, G. Franke, M. Hagen-Eggert, *et al.*, “In vivo Fourier-domain full-field OCT of the human retina with 15 million A-lines/s,” *Opt. Lett.* **35**(20), 3432–3434 (2010).
11. D. J. Fechtig, B. Grajciar, T. Schmoll, *et al.*, “Line-field parallel swept source MHz OCT for structural and functional retinal imaging,” *Biomed. Opt. Express* **6**(3), 716–735 (2015).
12. L. Ginner, A. Kumar, D. Fechtig, *et al.*, “Noniterative digital aberration correction for cellular resolution retinal optical coherence tomography *in vivo*,” *Optica* **4**(8), 924–931 (2017).
13. L. Ginner, T. Schmoll, A. Kumar, *et al.*, “Holographic line field en-face OCT with digital adaptive optics in the retina *in vivo*,” *Biomed. Opt. Express* **9**(2), 472 (2018).
14. V. P. Pandiyan, X. Jiang, A. Maloney-Bertelli, *et al.*, “High-speed adaptive optics line-scan OCT for cellular-resolution optoretinography,” *Biomed. Opt. Express* **11**(9), 5274–5296 (2020).
15. V. P. Pandiyan, X. Jiang, J. A. Kuchenbecker, *et al.*, “Reflective mirror-based line-scan adaptive optics OCT for imaging retinal structure and function,” *Biomed. Opt. Express* **12**(9), 5865–5880 (2021).
16. V. P. Pandiyan, A. Maloney-Bertelli, J. A. Kuchenbecker, *et al.*, “The optoretinogram reveals the primary steps of phototransduction in the living human eye,” *Sci. Adv.* **6**(37), eabc1124 (2020).
17. L. Han, B. Tan, Z. Hosseinaee, *et al.*, “Line-scanning SD-OCT for *in-vivo*, non-contact, volumetric, cellular resolution imaging of the human cornea and limbus,” *Biomed. Opt. Express* **13**(7), 4007–4020 (2022).
18. K. Chen, W. Song, L. Han, *et al.*, “Powell lens-based line-field spectral domain optical coherence tomography system for cellular resolution imaging of biological tissue,” *Biomed. Opt. Express* **14**(5), 2003–2014 (2023).
19. J. S. Penn, A. Madan, R. B. Caldwell, *et al.*, “Vascular endothelial growth factor in eye disease,” *Prog. Retinal Eye Res.* **27**(4), 331–371 (2008).
20. S. R. Flaxman, R. R. A. Bourne, S. Resnikoff, *et al.*, “Global causes of blindness and distance vision impairment 1990–2020: a systematic review and meta-analysis,” *Lancet Global Health* **5**(12), e1221–e1234 (2017).
21. C. Dalmon, T. C. Porco, T. M. Lietman, *et al.*, “The Clinical Differentiation of Bacterial and Fungal Keratitis: A Photographic Survey,” *Invest. Ophthalmol. Visual Sci.* **53**(4), 1787–1791 (2012).
22. M. B. Muijzer, P. A. W. J. Schellekens, H. J. M. Beckers, *et al.*, “Clinical applications for intraoperative optical coherence tomography: a systematic review,” *Eye* **36**(2), 379–391 (2022).
23. Y. Jian, K. Wong, and M. V. Sarunic, “Graphics processing unit accelerated optical coherence tomography processing at megahertz axial scan rate and high resolution video rate volumetric rendering,” *J. Biomed. Opt.* **18**(02), 1 (2013).
24. K. Neuhaus, S. Ni, S. Khan, *et al.*, “Real-time line-field OCT using low-cost high-speed camera,” in *Optical Coherence Tomography and Coherence Domain Optical Methods in Biomedicine XXVII* (SPIE, 2023), Vol. 12367, pp. 61–67.
25. Mitutoyo America Corporation, “MICROSCOPE UNITS AND OBJECTIVES, Catalog No. E4191-378\_010611,” (2016).
26. J. A. Izatt, M. A. Choma, and A.-H. Dhalla, “Theory of Optical Coherence Tomography,” in *Optical Coherence Tomography* (Springer, Cham, 2015), pp. 65–94.
27. W. Drexler and J. G. Fujimoto, eds., *Optical Coherence Tomography: Technology and Applications*, 2nd ed. (Springer International Publishing, 2015).
28. S. Borkovkina, A. Camino, W. Janpongnsri, *et al.*, “Real-time retinal layer segmentation of OCT volumes with GPU accelerated inferencing using a compressed, low-latency neural network,” *Biomed. Opt. Express* **11**(7), 3968 (2020).
29. J. Xu, K. Wong, Y. Jian, *et al.*, “Real-time acquisition and display of flow contrast using speckle variance optical coherence tomography in a graphics processing unit,” *J. Biomed. Opt.* **19**(02), 1 (2014).
30. J. Schindelin, I. Arganda-Carreras, E. Frise, *et al.*, “Fiji: an open-source platform for biological-image analysis,” *Nat. Methods* **9**(7), 676–682 (2012).
31. P. Virtanen, R. Gommers, T. E. Oliphant, *et al.*, “SciPy 1.0: Fundamental Algorithms for Scientific Computing in Python,” *Nat. Methods* **17**(3), 261–272 (2020).
32. C. R. Harris, K. J. Millman, S. J. van der Walt, *et al.*, “Array programming with NumPy,” *Nature* **585**(7825), 357–362 (2020).
33. . “Image Deconvolution — skimage v0.12dev docs,” [http://scikit-image.org/docs/dev/auto\\_examples/plot\\_restoration.html](http://scikit-image.org/docs/dev/auto_examples/plot_restoration.html).
34. M. D. Hanwell, C. J. Harris, A. Genova, *et al.*, “Tomviz: Open Source Platform Connecting Image Processing Pipelines to GPU Accelerated 3D Visualization,” *Microsc. Microanal.* **25**(S2), 408–409 (2019).
35. J. M. Bradley, J. Vranka, C. M. Colvis, *et al.*, “Effect of matrix metalloproteinases activity on outflow in perfused human organ culture,” *Invest. Ophthalmol. Visual Sci.* **39**, 2649–2658 (1998).
36. D. H. Johnson and R. C. Tschumper, “Human trabecular meshwork organ culture. A new method,” *Invest. Ophthalmol. Visual Sci.* **28**, 945–953 (1987).
37. J. A. Izatt, M. D. Kulkarni, Hsing-Wen Wang, *et al.*, “Optical coherence tomography and microscopy in gastrointestinal tissues,” *IEEE J. Sel. Top. Quantum Electron.* **2**(4), 1017–1028 (1996).
38. J. G. Fujimoto, C. Pitriss, S. A. Boppart, *et al.*, “Optical Coherence Tomography: An Emerging Technology for Biomedical Imaging and Optical Biopsy,” *Neoplasia* **2**(1-2), 9–25 (2000).
39. R. Leitgeb, C. K. Hitzenberger, and A. F. Fercher, “Performance of fourier domain vs. time domain optical coherence tomography,” *Opt. Express* **11**(8), 889–894 (2003).
40. Z. Yaqoob, J. Wu, and C. Yang, “Spectral domain optical coherence tomography: a better OCT imaging strategy,” *BioTechniques* **39**(6S), S6–S13 (2005).

41. "ANSI Z80.36-2021 - Ophthalmics - Light Hazard Protection for Ophthalmic Instruments," [https://webstore.ansi.org/standards/vc%20\(asc%20z80\)/ansiz80362021](https://webstore.ansi.org/standards/vc%20(asc%20z80)/ansiz80362021).
42. M. Newville, T. Stensitzki, D. B. Allen, *et al.*, "LMFIT: Non-Linear Least-Square Minimization and Curve-Fitting for Python," (2014).
43. S. Aumann, S. Donner, J. Fischer, *et al.*, eds. (Springer International Publishing, 2019), pp. 59–85.
44. T. S. Acott, M. J. Kelley, K. E. Keller, *et al.*, "Intraocular Pressure Homeostasis: Maintaining Balance in a High-Pressure Environment," *J. Ocul. Pharmacol. Ther.* **30**(2-3), 94–101 (2014).
45. K. Wang, M. A. Johnstone, C. Xin, *et al.*, "Estimating Human Trabecular Meshwork Stiffness by Numerical Modeling and Advanced OCT Imaging," *Invest. Ophthalmol. Visual Sci.* **58**(11), 4809–4817 (2017).
46. A. Karimi, S. Khan, R. Razaghi, *et al.*, "Developing an experimental-computational workflow to study the biomechanics of the human conventional aqueous outflow pathway," *Acta Biomater.* **164**, 346–362 (2023).
47. K. Bizheva, B. Tan, B. MacLellan, *et al.*, "In-vivo imaging of the palisades of Vogt and the limbal crypts with sub-micrometer axial resolution optical coherence tomography," *Biomed. Opt. Express* **8**(9), 4141–4151 (2017).
48. S. Patel and L. Tuchenco, "The refractive index of the human cornea: A review," *Contact Lens and Anterior Eye* **42**(5), 575–580 (2019).
49. S. Bohn, K. Sperlich, T. Stahnke, *et al.*, "Multiwavelength confocal laser scanning microscopy of the cornea," *Biomed. Opt. Express* **11**(10), 5689–5700 (2020).
50. S. Khan, K. Neuhaus, O. Thaware, *et al.*, "Visible-light optical coherence microscopy for corneal imaging," in *Optical Coherence Tomography and Coherence Domain Optical Methods in Biomedicine XXVII* (SPIE, 2023), Vol. 12367, pp. 87–90.
51. S. Khan, K. Neuhaus, O. Thaware, *et al.*, "Corneal imaging with blue-light optical coherence microscopy," *Biomed. Opt. Express* **13**(9), 5004–5014 (2022).